Acta Mech 226:123–135 (2015)
DOI 10.1007/s00707-014-1166-5

M. R. Moosavi · A. Khelil

Isogeometric meshless finite volume method in nonlinear elasticity

Received: 21 February 2014 / Revised: 3 May 2014 / Published online: 10 June 2014

Abstract An isogeometric meshless finite volume method has been presented to solve some nonlinear problems in elasticity. A non-uniform rational B-spline isogeometric basis function is used to construct the shape function. High computational efficiency and precision are other benefits of the method. Solving some sample problems of thin-walled structures shows the good performance of this method.

1 Introduction

Many engineering problems of interest are inherently nonlinear. In solid mechanics, generally, two kinds of nonlinearities are encountered, viz. material and geometrical nonlinearities. A typical material nonlinearity is the plastic response of many kinds of materials, such as the metals. Geometrical nonlinearity becomes significant when the solid undergoes a large deformation, leading to a considerable variation in the shape of the solid that cannot be neglected. Research into large deformation analysis began many years ago. Kohnke [1] and Haisler et al. [2] introduced a mathematical programming approach for the analysis of geometrically nonlinear structural behavior, and applied it to the analysis of frame structures. De Freitas and Smith [3,4] also proposed a mathematical programming approach for the elastoplastic solutions of large displacement problems, and applied it to the analysis of planar structures. Many other approaches based on the traditional Newton–Raphson iteration were also introduced in the last decade. Boisse et al. [5] presented a fully nonlinear shell theory including both the membrane and bending components in the field of large elastoplastic deformations, and applied it to the analysis of thin shells. Lee [6] performed a three-dimensional large-strain non-steady-state elastoplastic finite element analysis for the flat rolling process. Basar and Itskov [7] introduced a refined constitutive and finite element formulation for arbitrary shell structures undergoing large elastoplastic deformations. Brünig [8] proposed an efficient framework for a nonlinear finite element procedure for the rate-independent finite strain analysis of solids undergoing large elastic-isochoric plastic deformations. All these analyses were based on the finite element method (FEM).

Meshless methods have attracted more and more attention from researchers, and some meshless methods have achieved remarkable progress. These meshless methods do not require a mesh to discretize the problem domain, because the approximate solution is constructed entirely based on a set of scattered nodes. A group of meshless methods have been developed including the smooth particle hydrodynamics (SPH) [9], the diffuse element method (DEM) [10], the element-free Galerkin (EFG) method [11], the reproducing kernel particle method (RKPM) [12] the point interpolation method (PIM) [13,14]. Liu [14] grouped these existing meshless

---

M. R. Moosavi (✉)
Mechanical Engineering Department, South Dakota State University, Brookings, SD 57007-0294, USA
E-mail: mr.moosavi@yahoo.com

A. Khelil
University of Lorraine, IJL UMR CNRS 7198, 54600 Villers Les Nancy, France

methods into two different categories: meshless methods based on strong-forms of partial differential equations (PDEs) (e.g., SPH) and meshless methods based on weak-forms of PDEs (e.g., DEM, RKPM, EFG, PIM). Later, Liu and Gu [15] clarified the combination of the strong- and weak-forms [16] as the third category of the meshless methods. In order to alleviate the global integration background mesh, the meshless methods based on the local weak-forms have also been developed, for example, the meshless local Petrov–Galerkin (MLPG) method [17–21], and the local radial point interpolation method (LRPIM) [22–24]. Chen et al. [25–27], Liu et al. [28,29] and Li et al. [30] applied meshless methods, such as the RKPM, to large deformation analysis, and found that these methods are very effective in dealing with large material distortion. In these analyses, Lagrangian and updated Lagrangian reproducing kernel (RK) shape functions have been introduced to approximate the field variables. A material kernel function was introduced to deal with large material distortions, in order that the support of the kernel function covers the same set of nodes during the course of large deformation to avoid kernel instability. Chen et al. [27] also observed that the RKPM requires a relatively large kernel support to obtain an accurate solution in incompressible problems. The aforementioned RKPM, developed by Liu et al. [31–34], is one of the meshless methods that takes full advantage of the concept of having no mesh. The RKPM introduces a correction function to the kernel to correct the boundary error in SPH. The discretization of the kernel estimate in SPH assures neither zero-th nor first order consistency in a finite domain, unless the lumped mass (or lumped volume) is carefully selected, which is a very difficult task with irregular boundaries and arbitrary particle distributions. Thus, the basic idea of the RKPM is to formulate the discrete consistency that is lacking in SPH. It modifies the kernel by introducing a correction function to enhance its accuracy near, or on the boundary of the problem domain. Due to this correction function, the RKPM kernel function obtains the consistency conditions throughout the domain of the problem.

Isogeometric analysis is devoted to unify numerical procedures related to geometrical design and analysis by using a single framework where the same techniques are utilized in both procedures. These tasks have been performed independently with pre-processing programs based on CAD technologies and numerical solvers based on the mesh-based or meshless methods. Pre-processing includes CAD representation of physical prototypes, where a virtual model is obtained through a geometric translation from the actual model. In addition, node generation and imposition of boundary conditions and loads are also performed at this stage. However, it is observed that the grid obtained after the node generation is only an approximation of the CAD geometrical model and poor approximations may be observed depending on the basis functions adopted during the spatial discretization. Hence, meshing procedures for finite element analysis usually deteriorate the CAD geometry, which is taken as "exact" when compared to the actual geometrical model. The first step of a numerical analysis refers to the computational reproduction of a representative geometrical model using CAD technologies, which are also responsible for producing node information to be utilized in a meshless analysis. Although many technologies may be employed to represent general geometries computationally, one can observe that most of the commercial programs based on CAD adopt non-uniform rational B-splines (NURBS) as a basic tool. NURBS are very useful since they can exactly represent all conics such as circles, ellipses, parabolas and hyperbolas. An analysis procedure based on CAD formulation is referred to as isogeometric analysis. Isogeometric analysis offers the possibility of integrating meshless analysis with CAD tools by using B-spline and NURBS parameterizations. Another important aspect related to isogeometric analysis is associated to the isoparametric concept, since the solution space is represented with the same basis functions utilized to represent the geometry. The general concepts on isogeometric analysis were first introduced by Hughes et al. [35] and simulations have been carried out, where very good results are observed for several applications in the field of solid and fluid mechanics.

In the present work, a numerical meshless model based on the isogeometric analysis is presented. An equilibrium equation for three-dimensional large deformation is developed and the isoparametric approach applied on the equilibrium equation. Assembly and evaluation of the stiffness matrix and load vector at local and global levels are described utilizing analogies with the meshless method and relations among physical, parametric and parent fields are established. In order to verify the present formulation with respect to important computational aspects such as accuracy and efficiency, comparisons are performed considering results obtained here for nonlinear elasticity applications. All examples are modeled with NURBS solids, and the displacement formulation is adopted for the equilibrium description.

2 Governing equations

The governing differential equation for a linear elastic body can be obtained by

$$\sigma_{ij,j} + b_i = 0 \quad \text{in } \Omega \tag{1}$$

with the boundary conditions

$$u_i = \bar{u}_i \qquad \text{on } \Gamma_u \tag{2a}$$

$$t_i = \sigma_{ij} n_j = \bar{t}_i \quad \text{on } \Gamma_t \tag{2b}$$

where σ_{ij} is the Cauchy stress tensor, b_i is the body force in the initial configuration, Ω is the initial configuration, $\bar{u}_i$ is the prescribed displacements on the initial displacement boundary Γ_u, n_j is the unit vector outward normal to the initial boundary Γ, and $\bar{t}_i$ is the prescribed tractions on the initial traction boundary Γ_t. By considering large deformations, the Cauchy stress tensor in Eq. (1) can be rewritten as

$$\sigma_{ij} = \frac{1}{2} C_{klij} \left(\frac{\partial u_i}{\partial X_k} + \delta_{ik} \right) \left(\frac{\partial u_i}{\partial X_j} + \frac{\partial u_j}{\partial X_i} + \frac{\partial u_k}{\partial X_i} \frac{\partial u_k}{\partial X_j} \right) \left(\frac{\partial u_j}{\partial X_l} + \delta_{jl} \right), \tag{3}$$

where C_{klij} is the elasticity matrix, u is the displacement, and X is the position in the initial configuration. In other words, $\frac{1}{2}\left(\frac{\partial u_i}{\partial X_j} + \frac{\partial u_j}{\partial X_i} + \frac{\partial u_k}{\partial X_i}\frac{\partial u_k}{\partial X_j}\right)$ is the Lagrangian strain tensor, and $\frac{1}{2} C_{klij}\left(\frac{\partial u_i}{\partial X_j} + \frac{\partial u_j}{\partial X_i} + \frac{\partial u_k}{\partial X_i}\frac{\partial u_k}{\partial X_j}\right)$ is the second order Piola–Kirchhoff stress tensor.

NURBS are built from B-splines. The B-spline parametric space is local to "patches". Patches play the role of subdomains within which material models are assumed to be uniform. A knot vector in three dimensions is a set of coordinates in the parametric space, written, $\varXi = \{\xi_1, \xi_2, \ldots, \xi_{n+p+1}\}$, $\mathcal{H} = \{\eta_1, \eta_2, \ldots, \eta_{m+q+1}\}$ and $\mathcal{Z} = \{\zeta_1, \zeta_2, \ldots, \zeta_{l+r+1}\}$ where, $\xi_i, \eta_j, \zeta_k \in \mathbb{R}$ are the ith, jth and kth their knots, respectively, i, j, k are the knot indices, $i = 1, 2, \ldots, n+p+1$, $j = 1, 2, \ldots, m+q+1$, $k = 1, 2, \ldots, l+r+1$, p, q, r are the polynomial orders, and n, m, l are the number of basis functions which comprise the B-spline. Using NURBS approximation, the geometry and the trial function are

$$\mathbf{x}(\boldsymbol{\xi}) = \mathbf{R}^T(\boldsymbol{\xi})\,\mathbf{x}, \tag{4}$$

$$u(\mathbf{x}) = \mathbf{R}^{I^T}(\boldsymbol{\xi})\mathbf{u}^I + \mathbf{R}^{B^T}(\boldsymbol{\xi})\mathbf{u}^B, \tag{5}$$

where $\mathbf{R}^{I^T}(\boldsymbol{\xi})$ and $\mathbf{R}^{B^T}(\boldsymbol{\xi})$ are NURBS basis function relating to interior and boundary control points, respectively, which is defined as follows:

$$\mathbf{R}_{ijk}^{pqr}(\xi, \eta, \zeta) = \frac{N_{ip}(\xi) M_{jq}(\eta) L_{kr}(\zeta) w_{ijk}}{\sum_{\hat{i}=1}^{n} \sum_{\hat{j}=1}^{m} \sum_{\hat{k}=1}^{l} N_{\hat{i}p}(\xi) M_{\hat{j}q}(\eta) L_{\hat{k}r}(\zeta) w_{\hat{i}\hat{j}\hat{k}}}. \tag{6}$$

$\boldsymbol{\xi} = \{\xi, \eta, \zeta\}$ is a vector of parametric coordinates, and $\mathbf{u}$ is a vector containing control variable associated with the control point $\mathbf{x}$. $N_{ip}(\xi)$, $M_{jq}(\eta)$ and $L_{kr}(\zeta)$ are B-spline basis functions in ξ, η, and ζ directions, respectively, which can be defined as

$$N_{ip}(\xi) = \begin{cases} 1 & \text{if} \quad \xi_i \le \xi < \xi_{i+1} \\ 0 & \text{otherwise} \end{cases} \qquad p = 0, \tag{7}$$

$$N_{ip}(\xi) = \frac{\xi - \xi_i}{\xi_{i+p} - \xi_i} N_{i(p-1)}(\xi) + \frac{\xi_{i+p+1} - \xi}{\xi_{i+p+1} - \xi_{i+1}} N_{(i+1)(p-1)}(\xi) \quad p = 1, 2, \ldots, \tag{8}$$

$$M_{jq}(\eta) = \begin{cases} 1 & \text{if} \quad \eta_j \le \eta < \eta_{j+1} \\ 0 & \text{otherwise} \end{cases} \qquad q = 0, \tag{9}$$

$$M_{jq}(\eta) = \frac{\eta - \eta_j}{\eta_{j+q} - \eta_j} M_{j(q-1)}(\eta) + \frac{\eta_{j+q+1} - \eta}{\eta_{j+q+1} - \eta_{j+1}} M_{(j+1)(q-1)}(\eta) \quad q = 1, 2, \ldots, \tag{10}$$

$$L_{kr}(\zeta) = \begin{cases} 1 & \text{if} \quad \zeta_k \le \zeta < \zeta_{k+1} \\ 0 & \text{otherwise} \end{cases} \qquad r = 0, \tag{11}$$

$$L_{kr}(\zeta) = \frac{\zeta - \zeta_k}{\zeta_{k+r} - \zeta_k} L_{k(r-1)}(\zeta) + \frac{\zeta_{k+r+1} - \zeta}{\zeta_{k+r+1} - \zeta_{k+1}} L_{(k+1)(r-1)}(\zeta) \quad r = 1, 2, \ldots, \tag{12}$$

and w_{ijk} is weight of control points. Derivatives of the B-spline basis functions are represented in terms of B-spline lower order bases owing to the recursive definition of the basis functions. The derivative of the ith basis function with respect to the parametric coordinate is defined as

$$\frac{\mathrm{d}}{\mathrm{d}\xi}N_{ip}(\xi)=\frac{p}{\xi_{i+p}-\xi_i}N_{i(p-1)}(\xi)-\frac{p}{\xi_{i+p+1}-\xi_{i+1}}N_{(i+1)(p-1)}(\xi), \tag{13}$$

$$\frac{\mathrm{d}^k}{\mathrm{d}\xi^k}N_{ip}(\xi)=\frac{p}{\xi_{i+p}-\xi_i}\left(\frac{\mathrm{d}^{k-1}}{\mathrm{d}\xi^{k-1}}N_{i(p-1)}(\xi)\right)-\frac{p}{\xi_{i+p+1}-\xi_{i+1}}\left(\frac{\mathrm{d}^{k-1}}{\mathrm{d}\xi^{k-1}}N_{(i+1)(p-1)}(\xi)\right). \tag{14}$$

The derivatives of B-spline basis functions are defined over the same knot vector. Derivatives of NURBS basis functions are obtained according to the following expression:

$$\begin{aligned}\frac{\partial}{\partial\xi}R_{ijk}^{pqr}(\xi,\eta,\zeta)=&\left(\left(\frac{\mathrm{d}}{\mathrm{d}\xi}N_{ip}(\xi)\right)M_{jq}(\eta)L_{kr}(\zeta)w_{ijk}W(\xi,\eta,\zeta)\right.\\&\left.-N_{ip}(\xi)M_{jq}(\eta)L_{kr}(\zeta)w_{ijk}\frac{\partial}{\partial\xi}W(\xi,\eta,\zeta)\right)\Big/ W^2(\xi,\eta,\zeta),\end{aligned} \tag{15}$$

where

$$W(\xi,\eta,\zeta)=\sum_{\hat{i}=1}^{n}\sum_{\hat{j}=1}^{m}\sum_{\hat{k}=1}^{l}N_{\hat{i}p}(\xi)M_{\hat{j}q}(\eta)L_{\hat{k}r}(\zeta)w_{\hat{i}\hat{j}\hat{k}}. \tag{16}$$

To relate the control variables with the given boundary values, Eq. (5) can be collocated at a set of boundary points $\mathbf{x}_C$, $C=1,2,\ldots,n_B$, i.e.,

$$u(\mathbf{x}_C)=\mathbf{R}^{B^T}(\mathbf{x}_C)\mathbf{u}^C \quad \mathbf{x}_C\in\Gamma, \tag{17}$$

where Γ indicates the boundary of the problem. It is noted that the control points in NURBS approximation may not lie on the problem boundary, and thus, the boundary collocation or interpolation point $\mathbf{x}_C$ also may not coincide with the corresponding boundary control point $\mathbf{x}_B$. Equation (17) can be recast into a matrix form as

$$\mathbf{u}^B=\mathbf{T}^T\mathbf{u}^C \quad \mathbf{T}^T=\mathbf{R}^{B^T}(\mathbf{x}_C), \qquad \mathbf{x}_C\in\Gamma, \tag{18}$$

where $\mathbf{u}^C$ and $\mathbf{u}^B$ are vectors of boundary control variables and physical values at the discretized boundary collocation points. From Eq. (18), one has

$$\mathbf{u}^C=\mathbf{T}^{-T}\mathbf{u}^B. \tag{19}$$

Then a generalized displacement vector $\mathbf{u}$ can be constructed as

$$u=\begin{Bmatrix}\mathbf{u}^I\\ \mathbf{u}^B\end{Bmatrix}=\begin{bmatrix}I & 0\\ 0 & \mathbf{T}^T\end{bmatrix}\begin{Bmatrix}\mathbf{u}^I\\ \mathbf{u}^C\end{Bmatrix}. \tag{20}$$

It is also worthwhile to point out that there is no obligation that the boundary interpolation points $\mathbf{x}_C$ coincide with either the control points or the grid knots. The basic idea of the present method is to enable the control variables to produce exact values at boundary interpolation points and then provide a straightforward way to enforce the Dirichlet boundary conditions. This is realized by evaluating Eq. (17) at a set of boundary interpolation points $\mathbf{x}_C$. Clearly, it is quite flexible to choose $\mathbf{x}_C$ provided the transformation matrix $\mathbf{T}$ is well defined. Of course for convenience the grid knots can be chosen as the interpolation points if possible. In other cases, a set of boundary interpolation points can always be selected to construct the relationship of Eq. (18) and the proposed method is general and does not depend on a specific basis order. Based on Eq. (19), Eq. (5) becomes

$$u(\mathbf{x})=\mathbf{R}^{I^T}(\boldsymbol{\xi})\mathbf{u}^I+\mathbf{R}^{B^T}(\boldsymbol{\xi})\mathbf{u}^C=\mathbf{R}^{I^T}(\boldsymbol{\xi})\mathbf{u}^I+\mathbf{R}^{B^T}(\boldsymbol{\xi})\mathbf{T}^{-T}\mathbf{u}^B. \tag{21}$$

The finite volume (FV) discretization is based on the integral form of the equation over the control volume or sub-domain Ω_s. In other words, the FV discretization uses the integral form of Eq. (1) over the sub-domain Ω_s around node I as

$$\int_{\Omega_s}\left[\sigma_{ij,j}+b_i\right]\mathrm{d}\Omega=0. \tag{22}$$

Applying the divergence theorem to the first integral term gives

$$\int_{\partial\Omega_s} \sigma_{ij} n_j \mathrm{d}\Gamma + \int_{\Omega_s} b_i \mathrm{d}\Omega = 0, \tag{23}$$

where n_j is the outward normal to the local boundary $\partial\Omega_s$. At this point, the conservative nature of the FVM is established as the flux, stress σ_{ij}, is integrated over the local boundary $\partial\Omega_s$. Substituting Eq. (3) into Eq. (23), we obtain

$$\int_{\partial\Omega_s} \left[\frac{1}{2} C_{klij} \left(\frac{\partial u_i}{\partial X_k} + \delta_{ik} \right) \left(\frac{\partial u_i}{\partial X_j} + \frac{\partial u_j}{\partial X_i} + \frac{\partial u_k}{\partial X_i} \frac{\partial u_k}{\partial X_j} \right) \left(\frac{\partial u_j}{\partial X_l} + \delta_{jl} \right) n_j \right] \mathrm{d}\Gamma + \int_{\Omega_s} b_i \mathrm{d}\Omega = 0. \tag{24}$$

By considering the traction boundary conditions from Eq. (2) and imposing it in Eq. (24) leads to

$$\begin{aligned}
&\int_{L_s} \frac{1}{2} C_{klij} \left(\frac{\partial u_i}{\partial X_k} + \delta_{ik} \right) \left(\frac{\partial u_i}{\partial X_j} + \frac{\partial u_j}{\partial X_i} + \frac{\partial u_k}{\partial X_i} \frac{\partial u_k}{\partial X_j} \right) \left(\frac{\partial u_j}{\partial X_l} + \delta_{jl} \right) n_j \mathrm{d}\Gamma \\
&+ \int_{L_{su}} \frac{1}{2} C_{klij} \left(\frac{\partial u_i}{\partial X_k} + \delta_{ik} \right) \left(\frac{\partial u_i}{\partial X_j} + \frac{\partial u_j}{\partial X_i} + \frac{\partial u_k}{\partial X_i} \frac{\partial u_k}{\partial X_j} \right) \left(\frac{\partial u_j}{\partial X_l} + \delta_{jl} \right) n_j \mathrm{d}\Gamma \\
&+ \int_{L_{st}} \frac{1}{2} C_{klij} \left(\frac{\partial u_i}{\partial X_k} + \delta_{ik} \right) \left(\frac{\partial u_i}{\partial X_j} + \frac{\partial u_j}{\partial X_i} + \frac{\partial u_k}{\partial X_i} \frac{\partial u_k}{\partial X_j} \right) \left(\frac{\partial u_j}{\partial X_l} + \delta_{jl} \right) n_j \mathrm{d}\Gamma \\
&+ \int_{\Omega_s} b_i \mathrm{d}\Omega = 0.
\end{aligned} \tag{25}$$

Equation (25) represents a physical meaning in the balance law of the local sub-domain Ω_s as conventional FVM with the traction boundary conditions being enforced. Hence, it is called isogeometric meshless finite volume (IMFV) formulation of the equilibrium equation. To handle the geometric nonlinearity, the incremental formulation is usually used. For the reference (undeformed) configuration during a finite deformation, we have the following incremental relationships:

$$u_i^{t+\Delta t} = u_i + \Delta u_i, \tag{26}$$

where Δu_i is the increment of displacement. The displacement can be interpolated with the shape function as in Eq. (21),

$$u_i(\mathbf{x}) = \sum_{J=1}^{n} \mathbf{R}^{I^{(J)}}(\boldsymbol{\xi}) u_i^{I^{(J)}} + \sum_{K=1}^{m} \mathbf{R}^{B^{(K)}}(\boldsymbol{\xi}) \mathbf{T}^{-T} u_i^{B^{(K)}}, \tag{27}$$

where n and m are number of interior and boundary nodes, respectively. Now, Eq. (24) is discretized by substituting Eqs. (26) and (27):

$$\begin{aligned}
&-\sum_{J=1}^{n} \left[\int_{L_s} \frac{1}{2} C_{klij} \left(\frac{\partial \mathbf{R}^{I^{(J)}}}{\partial X_k} + \delta_{ik} \right) \left(\frac{\partial \mathbf{R}^{I^{(J)}}}{\partial X_j} + \frac{\partial \mathbf{R}^{I^{(J)}}}{\partial X_i} + \frac{\partial \mathbf{R}^{I^{(J)}}}{\partial X_i} \frac{\partial \mathbf{R}^{I^{(J)}}}{\partial X_j} \right) \left(\frac{\partial \mathbf{R}^{I^{(J)}}}{\partial X_l} + \delta_{jl} \right) n_j \mathrm{d}\Gamma \right] \Delta u_i^{I^{(J)}} \\
&-\sum_{K=1}^{m} \left[\int_{L_{su}} \frac{1}{2} C_{klij} \left(\frac{\partial \mathbf{R}^{B^{(K)}}}{\partial X_k} + \delta_{ik} \right) \left(\frac{\partial \mathbf{R}^{B^{(K)}}}{\partial X_j} + \frac{\partial \mathbf{R}^{B^{(K)}}}{\partial X_i} + \frac{\partial \mathbf{R}^{B^{(K)}}}{\partial X_i} \frac{\partial \mathbf{R}^{B^{(K)}}}{\partial X_j} \right) \left(\frac{\partial \mathbf{R}^{B^{(K)}}}{\partial X_l} + \delta_{jl} \right) n_j \mathrm{d}\Gamma \right] \Delta u_i^{B^{(K)}} \\
&-\sum_{K=1}^{m} \left[\int_{L_{st}} \frac{1}{2} C_{klij} \left(\frac{\partial \mathbf{R}^{B^{(K)}}}{\partial X_k} + \delta_{ik} \right) \left(\frac{\partial \mathbf{R}^{B^{(K)}}}{\partial X_j} + \frac{\partial \mathbf{R}^{B^{(K)}}}{\partial X_i} + \frac{\partial \mathbf{R}^{B^{(K)}}}{\partial X_i} \frac{\partial \mathbf{R}^{B^{(K)}}}{\partial X_j} \right) \left(\frac{\partial \mathbf{R}^{B^{(K)}}}{\partial X_l} + \delta_{jl} \right) n_j \mathrm{d}\Gamma \right] \Delta u_i^{B^{(K)}}
\end{aligned}$$

$$\begin{aligned}
&= \sum_{J=1}^{n}\left[\int\limits_{L_s} \frac{1}{2} C_{klij}\left(\frac{\partial \mathbf{R}^{I^{(J)}}}{\partial X_k}+\delta_{ik}\right)\left(\frac{\partial \mathbf{R}^{I^{(J)}}}{\partial X_j}+\frac{\partial \mathbf{R}^{I^{(J)}}}{\partial X_i}+\frac{\partial \mathbf{R}^{I^{(J)}}}{\partial X_i}\frac{\partial \mathbf{R}^{I^{(J)}}}{\partial X_j}\right)\left(\frac{\partial \mathbf{R}^{I^{(J)}}}{\partial X_l}+\delta_{jl}\right) n_j \mathrm{d}\Gamma\right] u_i^{I^{(J)}} \\
&+\sum_{K=1}^{m}\left[\int\limits_{L_{su}} \frac{1}{2} C_{klij}\left(\frac{\partial \mathbf{R}^{B^{(K)}}}{\partial X_k}+\delta_{ik}\right)\left(\frac{\partial \mathbf{R}^{B^{(K)}}}{\partial X_j}+\frac{\partial \mathbf{R}^{B^{(K)}}}{\partial X_i}+\frac{\partial \mathbf{R}^{B^{(K)}}}{\partial X_i}\frac{\partial \mathbf{R}^{B^{(K)}}}{\partial X_j}\right)\left(\frac{\partial \mathbf{R}^{B^{(K)}}}{\partial X_l}+\delta_{jl}\right) n_j \mathrm{d}\Gamma\right] u_i^{B^{(K)}} \\
&+\sum_{K=1}^{m}\left[\int\limits_{L_{st}} \frac{1}{2} C_{klij}\left(\frac{\partial \mathbf{R}^{B^{(K)}}}{\partial X_k}+\delta_{ik}\right)\left(\frac{\partial \mathbf{R}^{B^{(K)}}}{\partial X_j}+\frac{\partial \mathbf{R}^{B^{(K)}}}{\partial X_i}+\frac{\partial \mathbf{R}^{B^{(K)}}}{\partial X_i}\frac{\partial \mathbf{R}^{B^{(K)}}}{\partial X_j}\right)\left(\frac{\partial \mathbf{R}^{B^{(K)}}}{\partial X_l}+\delta_{jl}\right) n_j \mathrm{d}\Gamma\right] u_i^{B^{(K)}} \\
&+\int\limits_{\Gamma_{st}}\left[\frac{1}{2} C_{klij}\left(\frac{\partial \bar{u}_i}{\partial X_k}+\delta_{ik}\right)\left(\frac{\partial \bar{u}_i}{\partial X_j}+\frac{\partial \bar{u}_j}{\partial X_i}+\frac{\partial \bar{u}_k}{\partial X_i}\frac{\partial \bar{u}_k}{\partial X_j}\right)\left(\frac{\partial \bar{u}_j}{\partial X_l}+\delta_{jl}\right) n_j\right] \mathrm{d}\Gamma+\int\limits_{\Omega_s} b_i \mathrm{d}\Omega=0. \qquad (28)
\end{aligned}$$

It can be found that Eq. (28) is nonlinear because the right hand side of this equation is also a function of displacements. Hence, the Newton–Raphson iteration is often used to get results in the analyses of large deformation problems.

Equation (28) can be written as

$$\mathbf{K}\boldsymbol{\Delta}\mathbf{u}=\mathbf{f}, \qquad (29)$$

where

$$\begin{aligned}
K_{ij} &= -\sum_{J=1}^{n}\left[\int\limits_{L_s} \frac{1}{2} C_{klij}\left(\frac{\partial \mathbf{R}^{I^{(J)}}}{\partial X_k}+\delta_{ik}\right)\left(\frac{\partial \mathbf{R}^{I^{(J)}}}{\partial X_j}+\frac{\partial \mathbf{R}^{I^{(J)}}}{\partial X_i}+\frac{\partial \mathbf{R}^{I^{(J)}}}{\partial X_i}\frac{\partial \mathbf{R}^{I^{(J)}}}{\partial X_j}\right)\left(\frac{\partial \mathbf{R}^{I^{(J)}}}{\partial X_l}+\delta_{jl}\right) n_j \mathrm{d}\Gamma\right] \\
&-\sum_{K=1}^{m}\left[\int\limits_{L_{su}} \frac{1}{2} C_{klij}\left(\frac{\partial \mathbf{R}^{B^{(K)}}}{\partial X_k}+\delta_{ik}\right)\left(\frac{\partial \mathbf{R}^{B^{(K)}}}{\partial X_j}+\frac{\partial \mathbf{R}^{B^{(K)}}}{\partial X_i}+\frac{\partial \mathbf{R}^{B^{(K)}}}{\partial X_i}\frac{\partial \mathbf{R}^{B^{(K)}}}{\partial X_j}\right)\left(\frac{\partial \mathbf{R}^{B^{(K)}}}{\partial X_l}+\delta_{jl}\right) n_j \mathrm{d}\Gamma\right] \\
&-\sum_{K=1}^{m}\left[\int\limits_{L_{st}} \frac{1}{2} C_{klij}\left(\frac{\partial \mathbf{R}^{B^{(K)}}}{\partial X_k}+\delta_{ik}\right)\left(\frac{\partial \mathbf{R}^{B^{(K)}}}{\partial X_j}+\frac{\partial \mathbf{R}^{B^{(K)}}}{\partial X_i}+\frac{\partial \mathbf{R}^{B^{(K)}}}{\partial X_i}\frac{\partial \mathbf{R}^{B^{(K)}}}{\partial X_j}\right)\left(\frac{\partial \mathbf{R}^{B^{(K)}}}{\partial X_l}+\delta_{jl}\right) n_j \mathrm{d}\Gamma\right]
\end{aligned}$$

$$(30)$$

is the stiffness matrix, $\Delta\mathbf{u}$ is the increment of displacement vector, and

$$\begin{aligned}
f_i &= \sum_{J=1}^{n}\left[\int\limits_{L_s} \frac{1}{2} C_{klij}\left(\frac{\partial \mathbf{R}^{I^{(J)}}}{\partial X_k}+\delta_{ik}\right)\left(\frac{\partial \mathbf{R}^{I^{(J)}}}{\partial X_j}+\frac{\partial \mathbf{R}^{I^{(J)}}}{\partial X_i}+\frac{\partial \mathbf{R}^{I^{(J)}}}{\partial X_i}\frac{\partial \mathbf{R}^{I^{(J)}}}{\partial X_j}\right)\left(\frac{\partial \mathbf{R}^{I^{(J)}}}{\partial X_l}+\delta_{jl}\right) n_j \mathrm{d}\Gamma\right] u_i^{I^{(J)}} \\
&+\sum_{K=1}^{m}\left[\int\limits_{L_{su}} \frac{1}{2} C_{klij}\left(\frac{\partial \mathbf{R}^{B^{(K)}}}{\partial X_k}+\delta_{ik}\right)\left(\frac{\partial \mathbf{R}^{B^{(K)}}}{\partial X_j}+\frac{\partial \mathbf{R}^{B^{(K)}}}{\partial X_i}+\frac{\partial \mathbf{R}^{B^{(K)}}}{\partial X_i}\frac{\partial \mathbf{R}^{B^{(K)}}}{\partial X_j}\right)\left(\frac{\partial \mathbf{R}^{B^{(K)}}}{\partial X_l}+\delta_{jl}\right) n_j \mathrm{d}\Gamma\right] u_i^{B^{(K)}} \\
&+\sum_{K=1}^{m}\left[\int\limits_{L_{st}} \frac{1}{2} C_{klij}\left(\frac{\partial \mathbf{R}^{B^{(K)}}}{\partial X_k}+\delta_{ik}\right)\left(\frac{\partial \mathbf{R}^{B^{(K)}}}{\partial X_j}+\frac{\partial \mathbf{R}^{B^{(K)}}}{\partial X_i}+\frac{\partial \mathbf{R}^{B^{(K)}}}{\partial X_i}\frac{\partial \mathbf{R}^{B^{(K)}}}{\partial X_j}\right)\left(\frac{\partial \mathbf{R}^{B^{(K)}}}{\partial X_l}+\delta_{jl}\right) n_j \mathrm{d}\Gamma\right] u_i^{B^{(K)}} \\
&+\int\limits_{\Gamma_{st}}\left[\frac{1}{2} C_{klij}\left(\frac{\partial \bar{u}_i}{\partial X_k}+\delta_{ik}\right)\left(\frac{\partial \bar{u}_i}{\partial X_j}+\frac{\partial \bar{u}_j}{\partial X_i}+\frac{\partial \bar{u}_k}{\partial X_i}\frac{\partial \bar{u}_k}{\partial X_j}\right)\left(\frac{\partial \bar{u}_j}{\partial X_l}+\delta_{jl}\right) n_j\right] \mathrm{d}\Gamma \\
&+\int\limits_{\Omega_s} b_i \mathrm{d}\Omega \qquad (31)
\end{aligned}$$

is the force vector.

3 Numerical examples

The proposed method is evaluated by the following examples. Those are presented to illustrate the implementation, accuracy and efficiency of the present IMFVM approach in nonlinear problems.

Example 1 Large deformation of 3-D cantilever beam subjected to end shear

A cantilever beam with length l and a transverse load is considered, $l = 10$ m, $h = 2$ m and $b = 0.1$ m, as shown in Fig. 1. The large deformation analysis is performed and the beam is subjected to a distributed vertical loading, which is fixed, along the right end with $P = 1/\text{Unit}$. The analysis is carried out using N incremental load steps, and the load-scaling factor is $\beta = 10$. It means that at the kth loading step, the distributed loading is $P_k = \beta k P/\text{Unit}$.

The above developed IMFVM formulation is used to solve this problem. Thirty-three regularly distributed field nodes are firstly used. For comparison, the results obtained by the FEM using the total Lagrangian (TL) and bi-linear elements with the same number of nodes (33 nodes) are also presented. All these results are compared with the reference FEM solution with 738 (41×18) nodes. In addition, the FEM results using 369 (41×9) nodes and loading steps $N = 8$. Table 1 lists vertical displacements at Point A obtained by the IMFVM method and the FEM. In both methods, 33 nodes are used. A sample of node distribution used in the IMFVM is shown in Fig. 2. The computational errors are also listed in this table. It is found that the present IMFVM formulation leads to more accurate results than FEM when the same numbers of nodes are used. This demonstrates that the IMFVM method has higher accuracy than the FEM. It should be mentioned here that, in this paper, the common and standard nonlinear FEM formulation with bi-linear elements is used. In other words, for fair comparison, we did not use the special techniques that have been developed to improve the effectiveness of FEM for large deformation problems.

For studying the computational efficiency, the CPU times of IMFVM are obtained and listed in Table 2. The CPU time of the FEM using the TL is also listed in the same table. From Table 2, it is observed that the FEM (with the same number of nodes, i.e., 33 nodes) needs less computational time because its interpolation and integration are very simple. However, the CPU time of the FEM shown in Table 2 does not include the computational cost in the preprocessing, which is usually computationally very expensive.

The computational cost must be considered together with the accuracy. A successful numerical method should obtain high accuracy at a lower computational cost. Therefore, Tables 1 and 2 should be studied

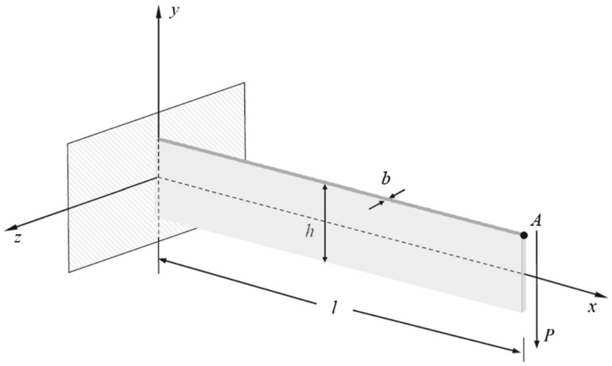

Fig. 1 A cantilever beam under a transverse load

Table 1 Vertical displacement at point A

Loading steps	$N = 1$	$N = 2$	$N = 3$	$N = 4$	$N = 5$	$N = 6$	$N = 7$	$N = 8$
Ref. solution, FEM 738 nodes								
$-v_A$	0.816	1.617	2.376	3.078	3.714	4.283	4.768	5.235
IMFVM 33 nodes								
$-v_A$	0.7936	1.5809	2.3318	3.0389	3.6887	4.2693	4.7580	5.2261
Error %	2.75	2.23	1.86	1.27	0.68	0.32	0.21	0.17
FEM 33 nodes								
$-v_A$	0.733	1.452	2.148	2.796	3.393	3.935	4.424	4.863
Error %	10.17	10.20	9.61	9.16	8.64	8.13	7.21	7.11

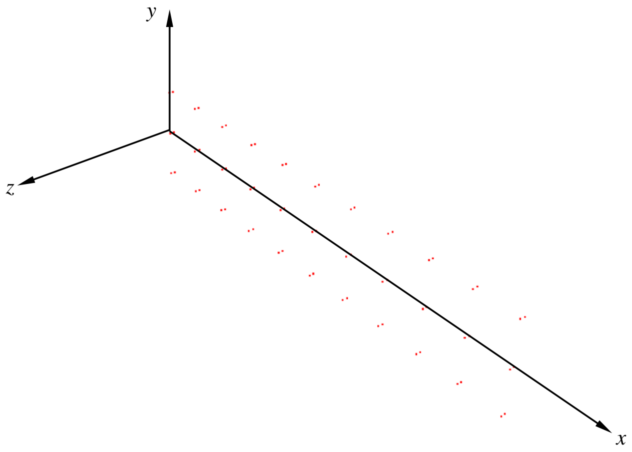

Fig. 2 A sample of node distribution in beam

Table 2 CPU time and the iteration steps

Loading steps	$N = 2$	$N = 4$	$N = 6$	$N = 8$
IMFVM 33 nodes				
CPU time	7.23	11.41	16.35	28.76
Iteration step	4	4	5	6
FEM 33 nodes				
CPU time	4.691	7.265	9.765	12.265
Iteration step	4	4	4	4

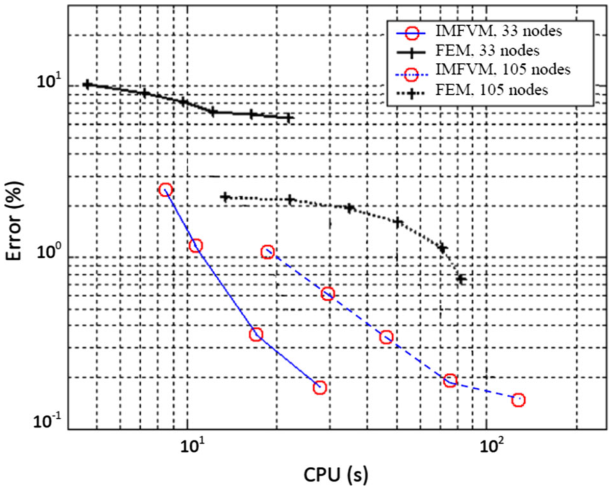

Fig. 3 CPU time versus computational error

together. Figure 3 plots the computational error versus the CPU time. For further comparison, the similar curves of IMFVM using 105 nodes and FEM using 105 nodes are also plotted in this figure. We can find that the IMFVM method has better efficiency than the FEM.

It should also be mentioned that, in this paper, the bilinear FE elements are used. Hence, the accuracy of the FEM is lower than of the IMFVM method, in which the higher order meshless shape functions are used. If the FE elements with a higher order are used, the accuracy of the FEM will be considerately improved, and therefore, the efficiency of the FEM will be also improved. In short, although the IMFVM has higher efficiency in this study, this is not always true. In fact, improving the efficiency of the meshless method is still a key issue in the development of meshless methods.

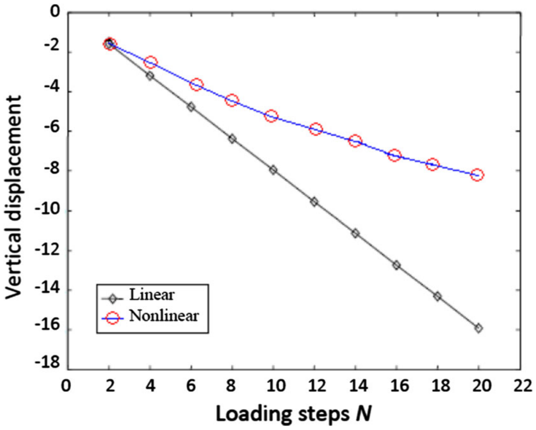

Fig. 4 Comparison between the linear and nonlinear results of the vertical displacement of point *A*

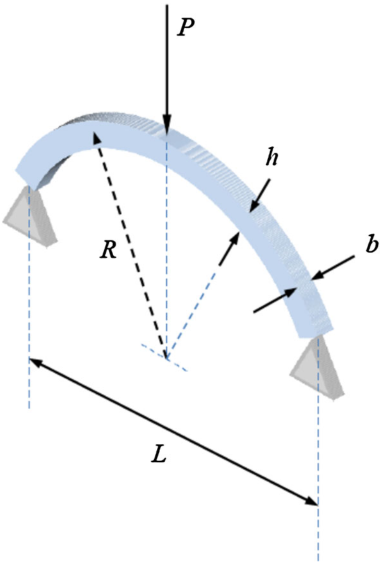

Fig. 5 A circular shallow arch under midspan concentrated load

To study the stability of the IMFVM method for nonlinear analyses, many loading steps are computed. It is found that very stable results obtained by the presented IMFVM method. It should be mentioned that the vertical deflection at the free end of the beam is already more than 5 times of the initial depth of the beam. It means that the IMFVM method is still stable even in the case of very large deformation. The deflection results obtained by IMFVM formulations versus the load steps for Point A are plotted in Fig. 4. For comparison, the results obtained by IMFVM method for the linear analysis are also plotted in the same figure. It can be seen that for this problem the nonlinear analysis makes the beam stiffer than the linear solutions as the load increases.

Example 2 Large deformation of a circular shallow arch

A pin supported elastic circular shallow arch is loaded with a concentrated force at its central point as shown in Fig. 5. For the arch, $\nu = 0$, $E = 68.948\,\mathrm{kN/mm^2}$, radius is $R = 10581.6$ mm, cross-section radial depth is $h = 79.2$ mm, and the width of the cross section is $b = 25.4$ mm. The span of the arch from pin to pin is $L = 2{,}540$ mm.

The arch is modeled with 2,761 nodes, which is similar to 2,500 quadrilateral elements. Figure 6 represents a sample of node distribution in the arc. In Fig. 7, the load displacement response, exhibiting snap-through behavior, is compared to results found by using 2,500 quadrilateral membrane elements in LS-DYNA [36]. The load displacement results are obtained by using a single node displacement control scheme using 115

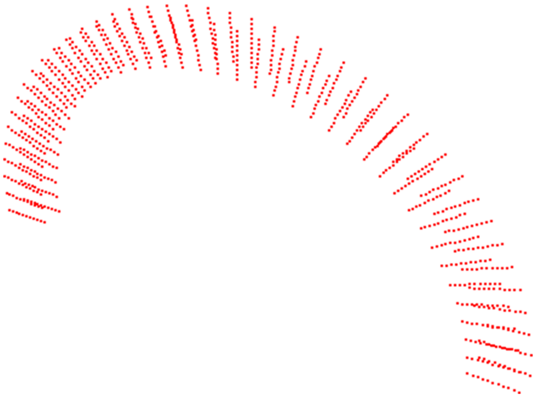

Fig. 6 Node distribution in circular shallow arch

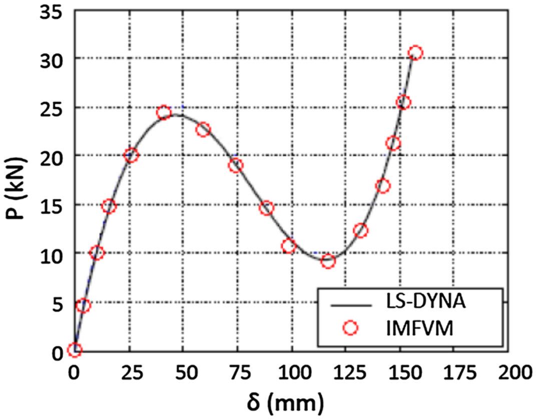

Fig. 7 Load displacement plot

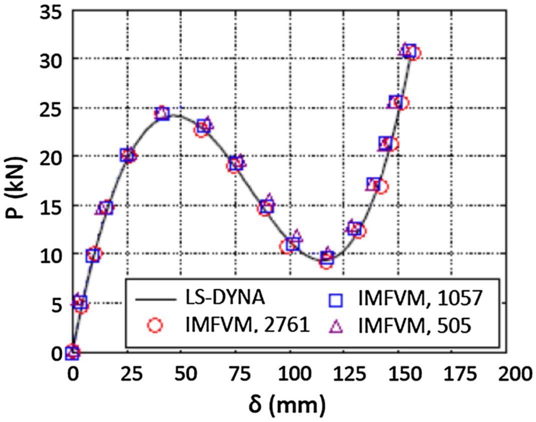

Fig. 8 Displacement convergence plot

displacement increments [37]. The agreement with LS-DYNA is very good. Numerical results are also shown in Fig. 8 illustrating the convergence of the meshless method with grid refinement. The analysis correctly captures the snap-through behavior.

Example 3 Square plate subjected to a concentrated load

A clamped square plate subjected to a concentrated load at the center of plate, Fig. 9, has been analyzed for its large deflection response. An 8-node brick element is used to model one quarter of the plate. Geometrical and material properties of the plate are: length of plate $L = 24$ in., thickness $b = 0.12$ in., Young's modulus $E =$

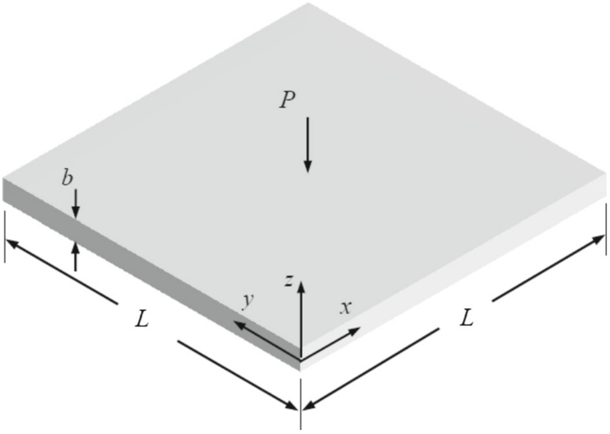

Fig. 9 A square plate subjected to a concentrated load

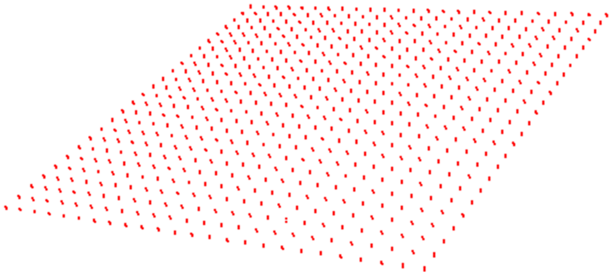

Fig. 10 Node distribution in square plate

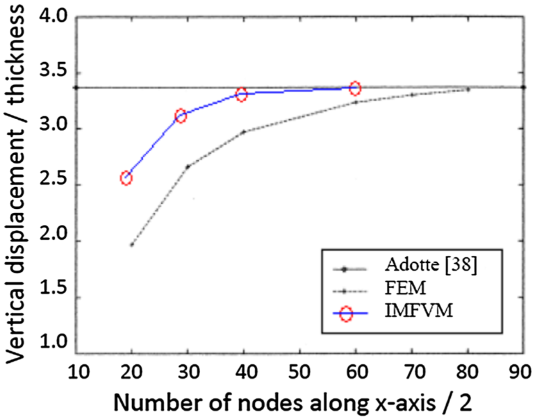

Fig. 11 Vertical displacement at central point of plate

10^7psi and Poisson ratio $\nu = 0.3$. The concentrated load is $P = 3{,}200Db/L^2$, where $D = Eb^3/12\left(1-\nu^2\right)$. A sample of the node distribution in the plate is shown in Fig. 10.

In both cases, two elements are considered through the thickness of the plates. Figure 11 shows the prediction of displacement at the loaded point by FEM and IMFVM. For the clamped plate, the finite difference solution reported by Adotte [38] has been used as the reference.

4 Conclusion

This paper presented the IMFVM applied to nonlinear elasticity problems. The IMFVM unifies the major advantages of meshless methods, finite volume method, and isogeometric analysis in one single scheme. In the local weak form (LWF) of the governing differential equation, a NURBS interpolation was used to form the approximations to the solution known as trial functions. Because of applying the NURBS approximation, this method does not have any singularity or ill-conditioning in calculation of shape function. Also, the method has a great computational precision. The IMFVM method was applied to and passed several test problems. Very good results from the method were obtained.

References

1. Kohnke, P.C.: Large deflection analysis of frame structures by fictitious forces. Int. J. Numer. Methods Eng. **12**, 1279–1294 (1978)
2. Haisler, W.E., Stricklin, J.A., Stebbins, F.J.: Development and evaluation of solution procedures for geometrically nonlinear structural analysis. AIAA J. **10**, 264–272 (1972)
3. De Freitas, J.A.T., Smith, D.L.: Existence, uniqueness and stability of elastoplastic solutions in the presence of large displacements. SM Arch. **9**, 433–450 (1984)
4. De Freitas, J.A.T., Smith, D.L.: Elastoplastic analysis of planar structures for large displacements. J. Struct. Mech. **12**, 419–445 (1984)
5. Boisse, P., Daniel, J.L., Ge'lin, J.C.: A combined membrane and bending model for the analysis of large elastic–plastic deformations of thin shells. In: Teodosiu, C., Raphanel, J.L., Rotterdam, S.F., Balkema, A.A. (eds.) Proceedings of the International Seminar MECMAT' 91 on Large Plastic Deformations: Fundamental Aspects and Applications to Metal Forming, Fontainebleau, France, pp. 369–376 (1993)
6. Lee, J.D.: A large-strain elastic–plastic finite element analysis of rolling process. Comput. Methods Appl. Mech. Eng. **161**, 315–347 (1998)
7. Basar, Y., Itskov, M.: Constitutive model and finite element formulation for large strain elasto-plastic analysis of shells. Computat. Mech. **23**, 466–481 (1999)
8. Brünig, M.: Formulation and numerical treatment of incompressibility constraints in large strain elastic–plastic analysis. Int. J. Numer. Methods Eng. **45**, 1047–1068 (1999)
9. Gingold, R.A., Moraghan, J.J.: Smooth particle hydrodynamics: theory and applications to non spherical stars. Mon. Notices R. Astron. Soc. **181**, 375–389 (1977)
10. Nayroles, B., Touzot, G., Villon, P.: Generalizing the finite element method: diffuse approximation and diffuse elements. Comput. Mech. **10**, 307–318 (1992)
11. Belytschko, T., Lu, Y.Y., Gu, L.: Element-free Galerkin methods. Int. J. Numer. Methods Eng. **37**, 229–256 (1994)
12. Liu, W.K., Jun, S., Zhang, Y.: Reproducing kernel particle methods. Int. J. Numer. Methods Eng. **20**, 1081–1106 (1995)
13. Liu, G.R., Gu, Y.T.: A point interpolation method for two-dimensional solids. Int. J. Numer. Methods Eng. **50**, 937–951 (2001)
14. Liu, G.R.: Mesh Free Methods: Moving Beyond the Finite Element Method. CRC Press, Boca Raton (2002)
15. Liu, G.R., Gu, Y.T.: An Introduction to Meshfree Methods and Their Programming. Springer, Berlin (2005)
16. Liu, G.R., Gu, Y.T.: Ameshfree method: meshfree weak–strong (MWS) form method, for 2-D solids. Comput. Mech. **33**(1), 2–14 (2003)
17. Atluri, S.N., Zhu, T.: A new meshless local Petrov–Galerkin (MLPG) approach in computational mechanics. Comput. Mech. **22**, 117–127 (1998)
18. Atluri, S.N., Kim, H.G., Cho, J.Y.: A critical assessment of the truly meshless local Petrov–Galerkin (MLPG), and local boundary integral equation (LBIE) methods. Comput. Mech. **24**, 348–372 (1999)
19. Atluri, S.N., Shen, S.P.: The Meshless Local Petrov–Galerkin (MLPG) Method. Tech Science Press, Encino (2002)
20. Gu, Y.T., Liu, G.R.: A meshless Local Petrov–Galerkin (MLPG) formulation for static and free vibration analyses of thin plates. CMES Comput. Model. Eng. Sci. **2**(4), 463–476 (2001)
21. Gu, Y.T., Liu, G.R.: A meshless local Petrov–Galerkin (MLPG) method for free and forced vibration analyses for solids. Comput. Mech. **27**(3), 188–198 (2001)
22. Gu, Y.T., Liu, G.R.: A local point interpolation method for static and dynamic analysis of thin beams. Comput. Methods Appl. Mech. Eng. **190**, 5515–5528 (2001)
23. Liu, G.R., Gu, Y.T.: A local radial point interpolation method (LRPIM) for free vibration analyses of 2-D solids. J. Sound Vib. **246**(1), 29–46 (2001)
24. Liu, G.R., Gu, Y.T.: Comparisons of two meshfree local point interpolation methods for structural analyses. Comput. Mech. **29**(2), 107–121 (2002)
25. Chen, J.S., Pan, C., Roque, C.M.O.L., Wang, H.P.: A Lagrangian reproducing kernel particle method for metal forming analysis. Comput. Mech. **22**, 289–307 (1998)
26. Chen, J.S., Pan, C., Wu, C.T.: Application of reproducing kernel particle method to large deformation contact analysis of elastomers. Rubber Chem. Technol. **71**, 191–213 (1998)
27. Chen, J.S., Pan, C., Wu, C.T., Liu, W.K.: Reproducing kernel particle methods for large deformation analysis of non-linear structures. Comput. Methods Appl. Mech. Eng. **139**, 195–227 (1996)
28. Liu, W.K., Jun, S.: Multiple-scale reproducing kernel particle methods for large deformation problems. Int. J. Numer. Methods Eng. **41**, 1339–1362 (1998)
29. Li, S., Hao, W., Liu, W.K.: Numerical simulations of large deformation of thin shell structures using meshfree methods. Comput. Mech. **25**, 102–116 (2000)
30. Li, S., Liu, W.K.: Numerical simulations of strain localization in inelastic solids using mesh-free methods. Int. J. Numer. Methods Eng. **48**, 1285–1309 (2000)
31. Liu, W.K., Jun, S., Zhang, Y.F.: Reproducing kernel particle methods. Int. J. Numer. Methods Fluids **20**, 1081–1106 (1995)
32. Liu, W.K., Jun, S., Li, S., Adee, J., Belytschko, T.: Reproducing kernel particle methods for structural dynamics. Int. J. Numer. Methods Eng. **38**, 1655–1679 (1995)

33. Jun, S., Liu, W.K., Belytschko, T.: Explicit reproducing kernel particle methods for large deformation problems. Int. J. Numer. Methods Eng. **41**, 137–166 (1998)
34. Liu, W.K., Chen, Y., Uras, R.A., Chang, C.T.: Generalized multiple scale reproducing kernel particle methods. Comput. Methods Appl. Mech. Eng. **139**, 91–157 (1996)
35. Hughes, T.J.R., Cottrell, J.A., Bazilevs, Y.: Isogeometric analysis: CAD, finite elements, NURBS, exact geometry and mesh refinement. Comput. Methods Appl. Mech. Eng. **194**, 4135–4195 (2005)
36. Hallquist, J.O.: LS-DYNA Theory Manual. Livermore Software Technology Corporation, Livermore, CA (2006)
37. Clarke, M.J., Hancock, G.J.: A study of incremental-iterative strategies for nonlinear analyses. Int. J. Numer. Methods Eng. **29**, 1365–1391 (1990)
38. Adotte, G.: Second order theory in orthotropic plates. Proceedings, Journal of the Structural Division, ASCE, 93 (ST5, proc. paper 5520), October 1967